



# An airblast hazard simulation engine for block caving sites

S.A. Galindo-Torres<sup>a,b,\*</sup>, S. Palma<sup>c</sup>, S. Quintero<sup>b</sup>, A. Scheuermann<sup>b</sup>, X. Zhang<sup>a</sup>, K. Krabbenhoft<sup>a</sup>, M. Ruest<sup>d</sup>, D. Finn<sup>e</sup>

<sup>a</sup> Department of Civil Engineering and Industrial Design, School of Engineering, University of Liverpool, UK

<sup>b</sup> Geotechnical Engineering Centre, School of Civil Engineering, The University of Queensland, Brisbane, QLD 4072, Australia

<sup>c</sup> Aix-Marseille Université, CNRS, IUSTI, France

<sup>d</sup> Goldcorp Limited, Canada

<sup>e</sup> Newcrest Mining Limited, Australia



## ARTICLE INFO

### Keywords:

Lattice Boltzmann method  
Discrete element method  
Airblast in block caving mining

## ABSTRACT

In this paper, a weakly compressible Lattice Boltzmann code is coupled with a realistic shape Discrete Element algorithm to create a simulation software to estimate the airspeed happening at airblast events in three dimensions. In an airblast event, air is compressed between falling rocks and the muckpile when the block caving method is used, creating potential hazardous air gusts compromising the safety of personnel and equipment. This work shows how the coupled code is capable of reproducing the key physical layers involved in this phenomenon such as the airspeeds attained by falling bodies in funnel geometries. After some validation examples, the code is used to evaluate the effect of the underground mine geometrical parameters on the potential airspeed. These examples show the potential of the software to be used by mining engineers to estimate accurately the impact of an airblast event.

## 1. Introduction

Airblast in block caving situations is a very dangerous situation with potential loss of life for operators and damage to mining equipment.<sup>1</sup> Airblasts occur when air pockets are present within the material that is currently being extracted through the drawpoints (Fig. 1).<sup>2</sup> As the material close to the drawpoints (defined as the muck-pile) becomes stagnant, the block falling at the top of the air gap will compress the air. Air will leave the empty space through any potential escape way at very high velocities, potentially endangering personnel and equipment.<sup>3</sup> One fatal example of an airblast accident happened at the Northparkes mine in Australia on November 24th, 1999, where four miners lost their lives.<sup>4</sup>

Airblast prevention has mostly been carried out at the site level by the installation of air obstructing wall structures to reduce the potential rise in airspeed and overpressure.<sup>5</sup> Actions aimed to mitigate effects of a potential airblast accident are difficult to apply at the planning stage due to the lack of appropriate modelling tools to simulate the problem. Modelling approaches have mostly focused on piston models, where the gas pressure is obtained from the adiabatic compression of an ideal gas.<sup>4,6</sup> This has the advantage of being a fast estimate for airspeed and overpressure but it loses the possibility of adding local features to the caving model, such as observation ducts and drawpoints. More

sophisticated models use machine learning techniques<sup>7</sup> to analyse and find patterns using global datasets found during airblast monitoring. One promising approach is to use the Discrete Element Method (DEM)<sup>8</sup> to model the rocks being extracted interacting with a Computational Fluid Dynamics (CFD) method representing the air to model the whole process. Recently this idea was used for the first time<sup>9</sup> to obtain important parameters for the air resistance of the muckpile. This study was carried out with circular elements in 2D using the PFC2D commercial code coupled with an incompressible fluid simulation code.

The present study presents a similar approach using DEM, but going a step further by simulating the whole process in 3D including a compressible gas characterized by the air sound speed and particles with more realistic shapes. Furthermore, it will include other cave characteristics such as a number of draw-points and observation ducts. The CFD method of choice is the Lattice Boltzmann Method (LBM), which as will be shown can deal with weakly compressible gases and is easily coupled with the DEM.<sup>10,11</sup>

The paper is structured as follows: Section 2 describes DEM-LBM coupling method in a succinct form and references are given for the readers interested in the details. Section 3 presents a series of validation examples including an experimental case. In Section 4 a parametric study is shown to illustrate the potential of the method to see the effect of different site parameters on a block caving situation. Finally, in

\* Corresponding author at: Department of Civil Engineering and Industrial Design, School of Engineering, University of Liverpool, UK.  
E-mail address: [s.torres@liverpool.ac.uk](mailto:s.torres@liverpool.ac.uk) (S.A. Galindo-Torres).

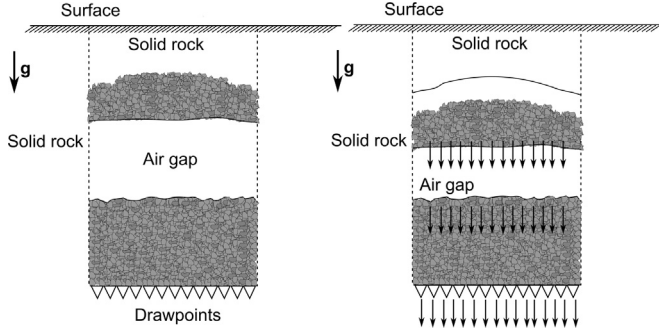


Fig. 1. Airblast hazard. In a block caving mining, the rocks fall down through the drawpoints. In the case there are air gaps between the falling block and the muckpile, the air will be compressed and released through any potential outlet at very high speeds, potentially endangering personnel and equipment.

Section 5 some conclusions and projections of the current work are presented.

## 2. The method

The simulation approach was introduced by the authors previously in Ref. 11. The fundamentals are based on the spheropolyhedra approach to model contact collision between DEM particles and how it can also be used to simplify the coupling with the LBM code. Here, a brief introduction to the method is included.

LBM is a grid based method solving the discrete Boltzmann equation. It divides the space in a cubic grid of side  $\delta_x$ .<sup>12</sup> The velocity space is also discretized by a set of velocities  $\vec{e}_i$  as seen in Fig. 2. A set of functions  $f_i(\vec{x})$  is assigned to the cell centered at  $\vec{x}$ . These functions represent the density of particles of fluid propagating in one of the different discrete directions. The macroscopic fluid density  $\rho$  and velocity  $\vec{u}$  are obtained from the following additions over the velocity space,

$$\begin{aligned}\rho(\vec{x}) &= \sum_i f_i(\vec{x}), \\ \vec{u}(\vec{x}) &= \frac{\sum_i f_i(\vec{x}) \vec{e}_i}{\rho(\vec{x})}.\end{aligned}\quad (1)$$

The discrete form of the Boltzmann equation governs the evolution of the  $f_i$  set. This equation contains both the dynamics of collision of particles as well as the transmission of information by streaming at each time step  $\delta_t$ ,

$$\begin{aligned}f_i(\vec{x} + \vec{e}_i \delta_t, t + \delta_t) &= f_i(\vec{x}, t) \\ &+ (1 - B_n) \left( \frac{1}{\tau} (f_i^{eq} - f_i) \right) + B_n \Omega_i^s,\end{aligned}\quad (2)$$

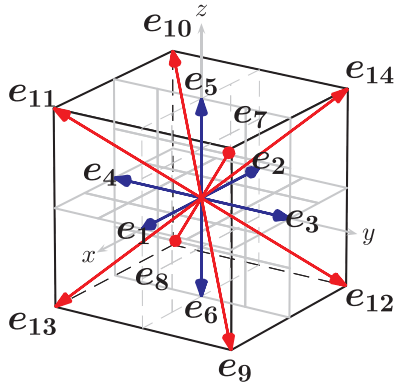


Fig. 2. The LBM cell of the D3Q15 showing the direction of each one of the 15 discrete velocities.

with  $B_n$  a volume occupation function which is important for moving boundaries as the ones presented when coupled with DEM,  $\tau$  is a characteristic dimensionless relaxation time related to the fluid viscosity,  $f_i^{eq}$  is an equilibrium function which should be reached at equilibrium conditions and finally  $\Omega_i^s$  is a collision term representing the momentum exchange with the moving boundary.

Calculating  $B_n$  is important to determine to correct momentum exchange with the DEM particles. In<sup>11</sup> it is shown how the form,

$$B_n(\varepsilon) = \frac{\varepsilon_n(\tau - 1/2)}{(1 - \varepsilon_n) + (\tau - 1/2)}, \quad (3)$$

which depends on the fraction of the cell volume occupied by the DEM particle  $\varepsilon_n$  is suitable. For the momentum exchange term ( $\Omega_i^s$ ) the following form is chosen,

$$\begin{aligned}\Omega_i^s &= [f_{i'}(\vec{x}, t) - f_i^{eq}(\rho, \vec{v}_p)] \\ &- [f_i(\vec{x}, t) - f_i^{eq}(\rho, \vec{v}_p)],\end{aligned}\quad (4)$$

where  $i'$  is the direction opposite to the  $i$ -th direction and  $\vec{v}_p$  is the velocity of the DEM particle at that point. With these two terms calculated, the force

$$\vec{F} = \frac{\delta_x^3}{\delta_t} \sum_n B_n \left( \sum_i \Omega_i^s \vec{e}_i \right), \quad (5)$$

and the torque over the DEM particle,

$$\vec{T} = \frac{\delta_x^3}{\delta_t} \sum_n \left[ (\vec{x}_n - \vec{x}_{CM}) \times B_n \left( \sum_i \Omega_i^s \vec{e}_i \right) \right], \quad (6)$$

are similarly calculated by summing the individual contributions over all the occupied cells where  $\varepsilon_n > 0$ .

As introduced by Chen and Doolen,<sup>13</sup> to recover Navier Stokes (NS) equations, the equilibrium function must be,

$$f_i^{eq} = \omega_i \rho \left( 1 + 3 \frac{\vec{e}_i \cdot \vec{u}}{C^2} + \frac{9(\vec{e}_i \cdot \vec{u})^2}{2C^4} - \frac{3u^2}{2C^2} \right), \quad (7)$$

where  $C = \delta_x / \delta_t$ . This version of LBM allows small changes in density and in fact can be used to model compressible gases as long as low Mach numbers are reached. In fact, the form for the equilibrium distribution will give a well defined relation for the fluid pressure  $p$  as a function of the density  $\rho$  in the NS equation,

$$p = \frac{C^2}{3} \rho, \quad (8)$$

where the factor 3 comes from the discretization of 15 velocities shown in Fig. 2. This implies that the speed of sound  $C_s = C / \sqrt{3}$ . Furthermore, it will be shown that it is practical to use this equation for situations where the gas is compressed by working with changes in pressure  $\Delta p = C_s^2 \Delta \rho$ , where the changes are relative to an equilibrium pressure and density values. By this equation, it can be seen that once  $\delta_x$  is fixed by the desired resolution, then the time step  $\delta_t$  must be chosen to obtain a realistic speed of sound. In this study  $C_s = 340$  m/s which in some cases imposed small values for  $\delta_t$  making some simulations challenging in terms of computational time.

One last property of the fluid is the kinetic viscosity  $\nu$  related to the relaxation time  $\tau$  by

$$\nu = \left( \tau - \frac{1}{2} \right) \frac{\delta_x^2}{3\delta_t}. \quad (9)$$

Once  $\delta_x$  and  $\delta_t$  are defined by the speed of sound, the  $\nu$  can only be controlled by the value of  $\tau$ . However, it is a well known fact that for low viscosities  $\tau \sim 1/2$  and the method becomes unstable. One very successful technique to avoid this instability and obtain an accurate response is to use the Large Eddy Simulation scheme within LBM.<sup>14</sup> In it a second viscosity is added to the one obtained from Eq. (9) to account

for the energy dissipation of the eddies presented at the unresolved scales during turbulent flow. The total relaxation time  $\tau_*$  is given by the formula,

$$\tau_* = \frac{1}{2}(\tau + \sqrt{\tau^2 + 6*Sc*Q/\rho}), \quad (10)$$

where  $Sc$  is the Smagorinsky constant (taken as 0.17) and

$$Q = \frac{\sqrt{\sum_{i,k=x,y,z} (f_i - f_i^{eq})^2 e_{i,k} e_{i,k}}}{C}. \quad (11)$$

As reported in the literature, this turbulence model can successfully simulate flows at a Reynolds number of 40,000 and beyond.<sup>14</sup>

Finally, the last component of the simulation engine is the representation of porous media within the LBM to model the muckpile. For this part, the percolation model presented in<sup>15</sup> is used by introducing a percolating parameter  $p_f$  which can be used to control the permeability of an LBM cell. It modifies Eq. (2) adding the following term at the right hand side

$$\dots + (1 - p_f)(f_i - f_i + (f_i - f_i^{eq})/\tau), \quad (12)$$

where  $p_f$  takes values between 0 (fully impermeable) and 1 (void space). For more details please refer to the cited paper.

### 3. Validation

The first validation example involves the use of the LES scheme for turbulence for the measurement of the drag coefficient  $C_d$  for a cylinder. A cylindrical DEM particle with a radius  $R$  of 21 cells is placed in the middle of a  $2100 \times 2100$  cells domain (Fig. 3). Velocity boundary conditions are applied on the left and right with a velocity equal to  $u = 0.1$  in lattice units (where  $\delta_x = \delta_t = 1$ ) and the force  $F$  over the cylinder is measured using Eq. (5). Several values for the Reynolds's number  $Re$  were tested by varying the viscosity  $\nu$  using Eq. (9). The formula for  $Re$  used is,

$$Re = \frac{2Ru}{\nu}, \quad (13)$$

and for the drag coefficient,

$$C_d = \frac{F}{\rho u^2 R}, \quad (14)$$

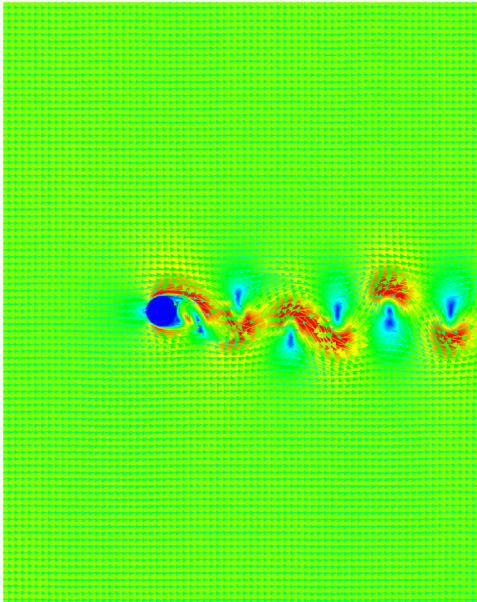


Fig. 3. Snapshot of the drag coefficient simulation for  $Re = 1000$ . The circular obstacle has a radius of 21 LBM cells and the domain has a size of  $2100 \times 2100$ .

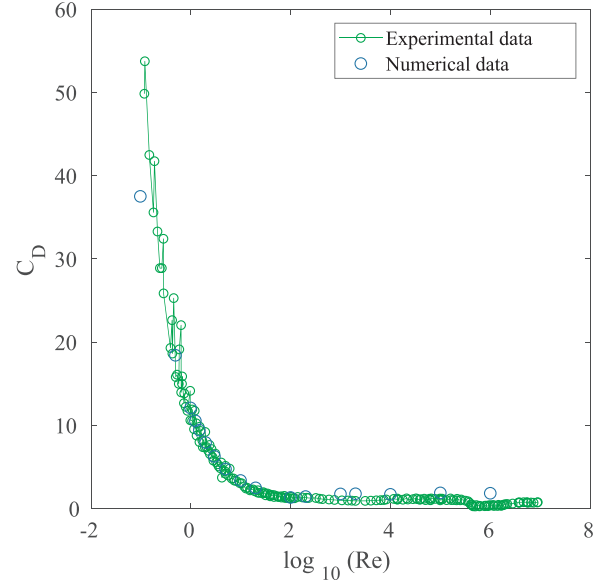


Fig. 4. Obtained value for the drag coefficient  $C_d$  as a function of  $Re$ .

where the value for the force is taken as a time average to eliminate the fluctuations that appear at high  $Re$  values due to the presence of eddies.

High values of  $Re$  produce values of  $\tau \sim 1/2$ . For instance for  $Re = 100000$ ,  $\tau = 0.50013$ . As can be seen in Fig. 4, even for this values of  $\tau$ , the LES scheme produces accurate and stable results when compared with experimental results used in previous numerical studies.<sup>16</sup>

A second validation is aimed at testing the compressibility nature given by Eq. (8). For it a cylindrical funnel of radius 0.15 m is filled with LBM gas and a DEM rectangular box of dimensions  $0.3 \text{ m} \times 0.3 \text{ m} \times 0.05 \text{ m}$  is placed at 0.44 m from the bottom. The density of the DEM particle is  $2000 \text{ kg/m}^3$  giving a weight of 88.2 N. The pressure over the LBM gas at equilibrium is the weight divided by the cross section of the funnel and is equal to 1247 Pa. The fluid has an initial density of  $1 \text{ kg/m}^3$  and a kinematic viscosity of  $2.0 \times 10^{-5} \text{ m}^2/\text{s}$ . The total simulated time is 1 s.

Fig. 5 shows the average pressure of the gas inside the funnel given by Eq. (8). As can be seen, after some vibrations, eventually it reaches the equilibrium value given by the piston weight. It is worth noting that

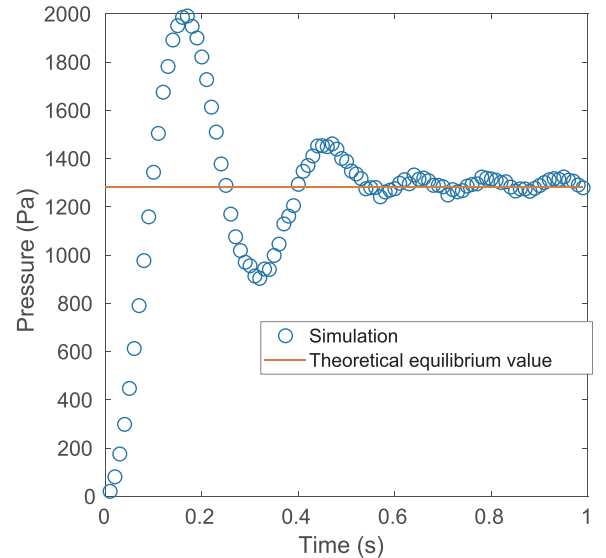


Fig. 5. Pressure of the gas in time compared with the equilibrium value which is equal to the weight of the piston divided by the funnel cross section area.

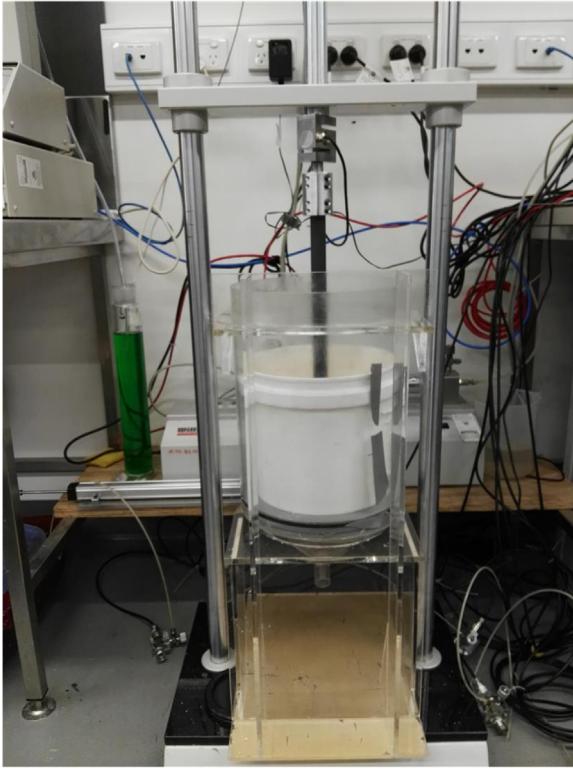


Fig. 6. Experimental setup to validate the flow code.

in no cell the density increased more 10% from the original value.

Finally, a small scale laboratory set-up was designed and manufactured to represent the geometric and physical conditions of a block cave draw point (Fig. 6). The purpose of this set-up is to create a physical model with conditions that simulate a small air blast and compare the results against numerical simulations with identical geometry and boundary conditions. The boundaries of the cave are formed by a cylinder and a funnel-shaped bottom. A piston guided by a rod is placed in the cylinder representing the falling rock mass. The piston is sealed against the cylinder walls using two o-rings which are lubricated with Vaseline to minimize friction. Air flow velocity can be measured directly at the outlet with a TurbulentFlow Instrumentation Cobra probe. The large diameter of the funnel is 395 mm, the height is 410 mm and the small air exhaust was 25 mm. The mass of the piston is 4.04 kg and two added weights of 3 kg and 4 kg were placed on top of it. An o-ring was placed around the piston to avoid air escapes from the top of the cylinder. This o-ring was lubricated to reduce friction. The airspeed probe is capable of measuring speeds in intervals of 2 ms. This is particularly important since due to the small size of the apparatus, the maximum speed is reached at a fraction of a second. At time equal 0 the piston is released and starts falling by its own weight, plus the weights put on top of it. Friction mitigates the piston speed. Airspeed is measured at the bottleneck exit with the probe. The piston eventually collides with the walls of the funnel when the bottleneck starts. Our DEM-LBM cannot reproduce this collision and therefore, only the data before this point was analysed. Taking this fact into account, for the weight of 3 kg, 1 s of experiment time was considered, whereas for the case of 4 kg a shorter time of 0.7 s was taken.

The same funnel of the previous validation case was used to simulate the experimental results and the weight of the piston was changed to reproduce the results. The speed of sound for Eq. (8) was taken as 340 m/s, the initial density of the LBM fluid was set to  $1 \text{ kg/m}^3$ , the kinetic viscosity was set as  $1.5 \times 10^{-5} \text{ m}^2/\text{s}$  and the grid size  $\delta_x$  as 2 mm. The dimensions of the cylindrical funnel are the same as with the experiment.

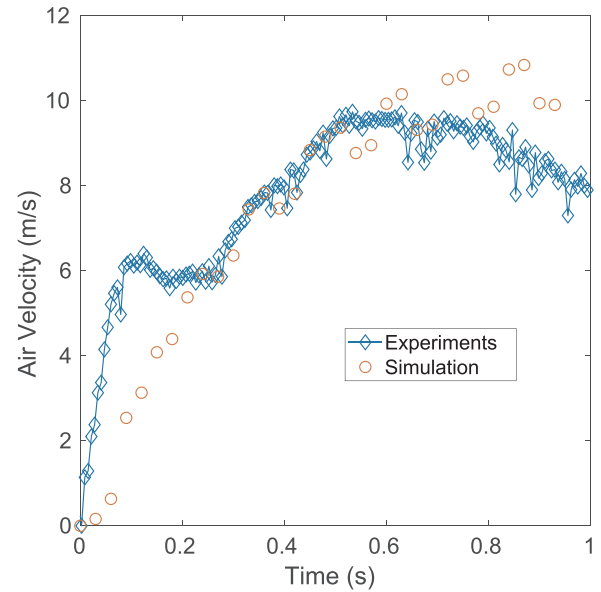


Fig. 7. Airspeed 4 mm below the lower exhaust for the weight of 3 kg compared with the simulation results.

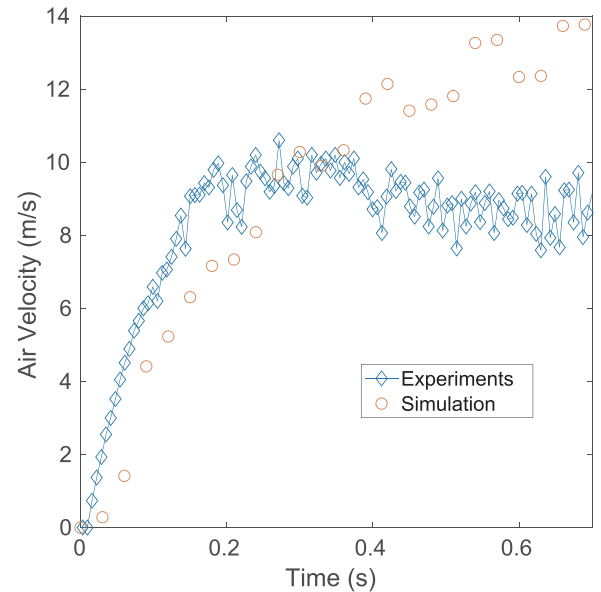


Fig. 8. Airspeed 4 mm below the lower exhaust for the weight of 4 kg compared with the simulation results.

Results are shown in Figs. 7 and 8. As can be seen the simulation airspeeds are close to the experimental data but overall they are higher. One of the reasons may be because of the uncertainty in the friction. Another reason may be the point of measure which is separated from the exhaust by just two LBM cells. Better resolutions may offer better matches, but unfortunately, the computational time offers a challenge, since due to the speed of sound, the time step  $\delta_t$  is in the order of  $10^{-6} \text{ s}$ .

#### 4. Results on an extraction cave geometry

To assess the capability of the code to simulate a block caving site, a rectangular domain with dimensions  $140 \times 120 \times 240 \text{ m}$  was used. An observation duct with a length of 20 m was introduced on the left as seen in Fig. 9 with an opening of 4 m. 25 draw-points are placed at the bottom of the domain in a square grid with a cylinder diameter of 12 m. At the end of both the observation duct and the draw-points, density



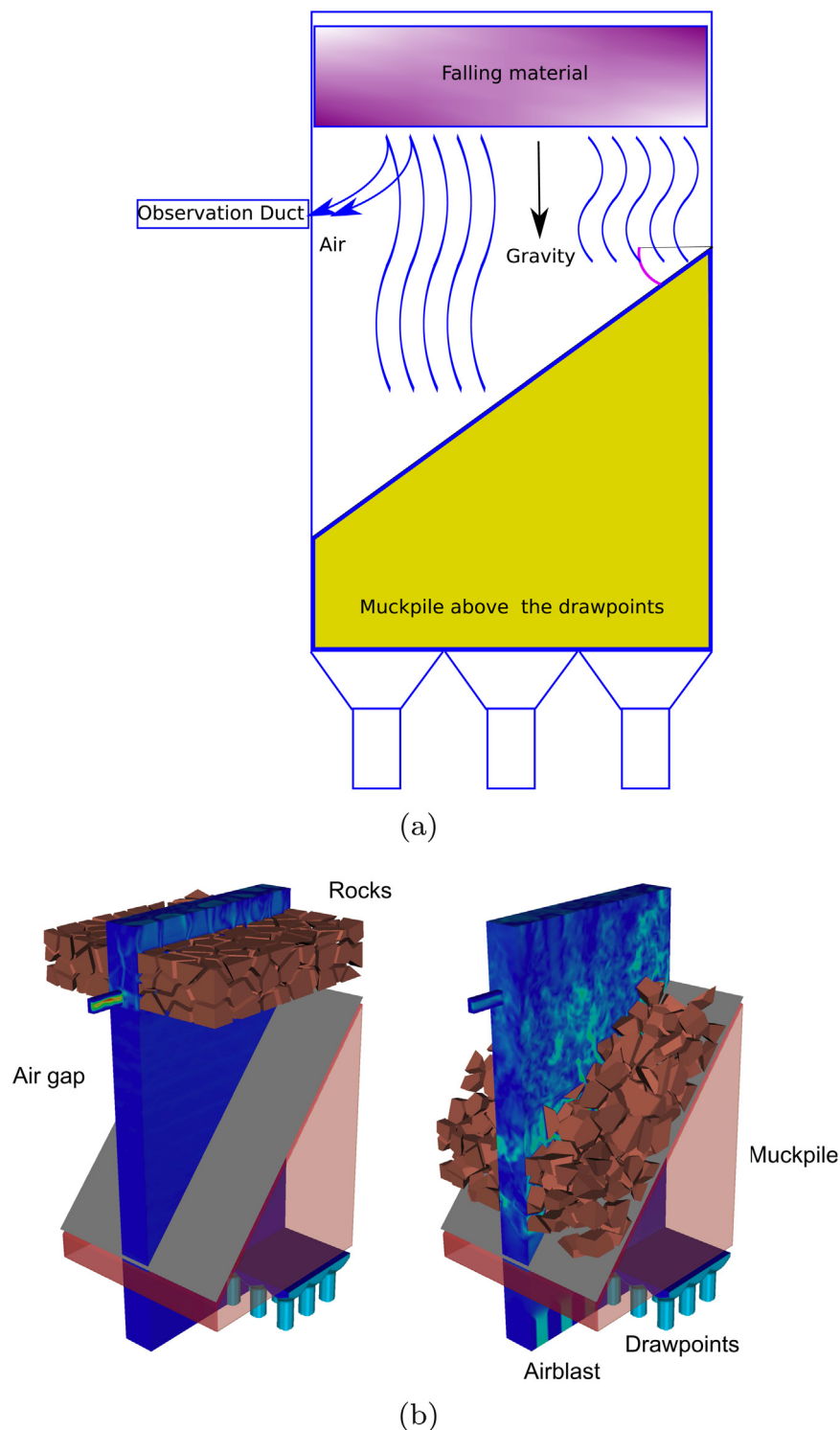


**Fig. 9.** Above, Block caving situation diagram. Below snapshots of the simulated excavation site with detailed drawpoints and the observation duct. The colormap in the middle is a cross section of the rectangular LBM domain. The colormap is proportional to the airspeed. The snapshots show the initial condition and the time frame after the rocks have settled on top of the muckpile. As can be seen the airspeed above the muckpile show signs of turbulence.

(pressure) boundary conditions were applied as explained in.<sup>17</sup> The muckpile is assumed to be a porous medium (with a permeability of  $10^{-8} \text{ m}^2$ ) with a slope of  $15^\circ$ . The falling mass is produced by a Voronoi tessellation of  $10 \times 10 \times 4$  cells with a thickness of 40 m where each Voronoi cell becomes a DEM particle. The particles are eroded so there is at least 1 m spacing between them as explained in Ref. 18. At the beginning of the simulation, the particles start falling by gravity.

Fig. 10 shows snapshots for different times of the airblast simulation

in the block caving geometry. As can be seen, the airspeed is higher at the observation duct than at the draw-points due to the muckpile. This corresponds to anecdotal reports for similar incidents (such as the fatal Northparkes accident) where the strong wind was felt inside the observation network and not at the draw-points. After the falling material passed the observation duct, the airspeed in it decreases.

To explore the dependence on the resolution, several values for the grid size were taken and the average airspeed was measured at the

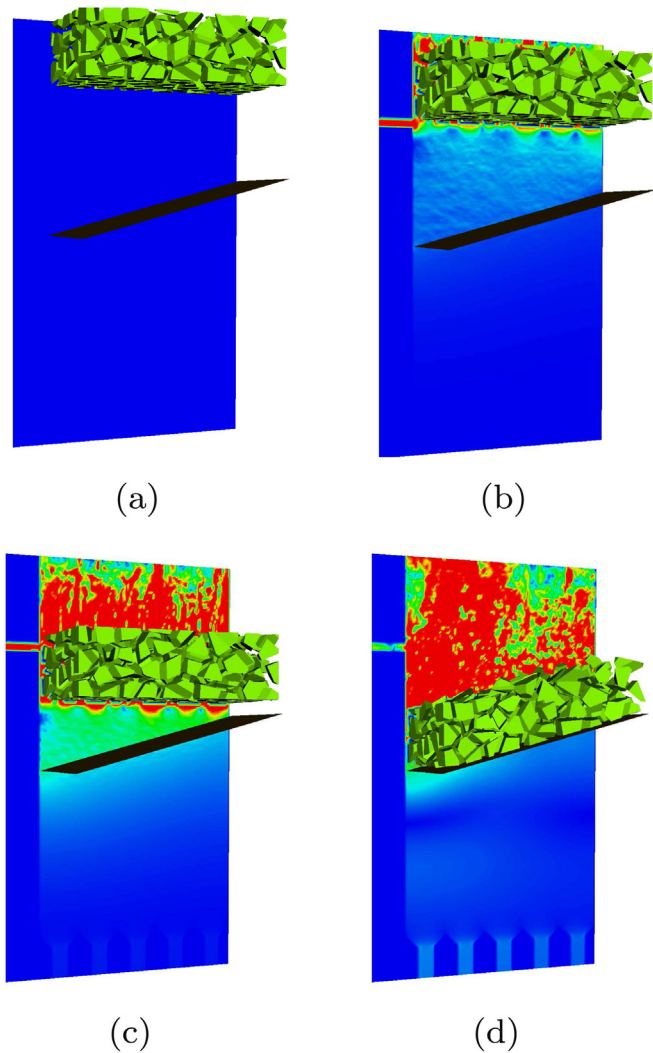


**Fig. 10.** Snapshots at different times of the airblast simulation. The colormap is proportional to the airspeed. At the initial condition a) the airspeed is zero and the rocks are released. In b) the falling rocks have attained some speed and the air is pushed downwards and through the observation ducts highlighted as red with the maximum airspeed (approximately 30 m/s. In c) the rocks are passing through the observation duct level. It is interesting to note that at this point several airspeed peaks are measured corresponding with the spaces between the falling rocks connecting with the observation duct. Finally at d) the rocks have settled at the top of the muckpile. The airspeed at the observation duct no longer has the peak value and the velocity at the drawpoints (at the domain's bottom) starts to increase.

observation duct. As can be seen in Fig. 11, the airspeed at the observation duct is sensible to the selection of  $\delta_x$ . However, it seems that for this particular problem, a choice of 0.5 m for the grid size seems to provide resolution independent results.

The next step is to conduct a parametric study on two parameters of the block caving geometry: the vertical position of the observation duct and the muckpile slope. Initially, the vertical position was altered by taking values from 50 m to 85 m (measured from the top of the domain). As can be seen in Fig. 12, the average airspeed depends highly on the position of this duct. Ducts that are close to the falling material experience less airspeed since the falling material has not picked up enough momentum. However, observation ducts close to the muckpile achieve almost twice as much air-speed due to the falling speed achieved. In every case, after the falling body passes the observation duct, there is a feedback due to the vacuum left by it (signalled by a negative airspeed) which also depends on the vertical position in a

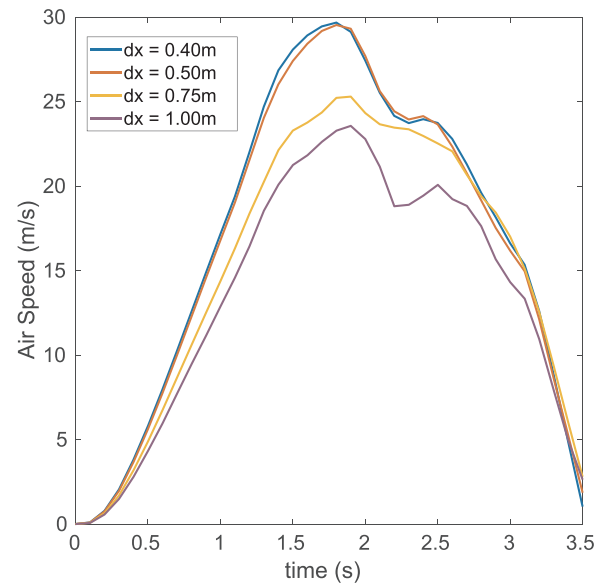


**Fig. 11.** Average airspeed in time inside the observation duct for different values of the grid size  $\delta_x$ .

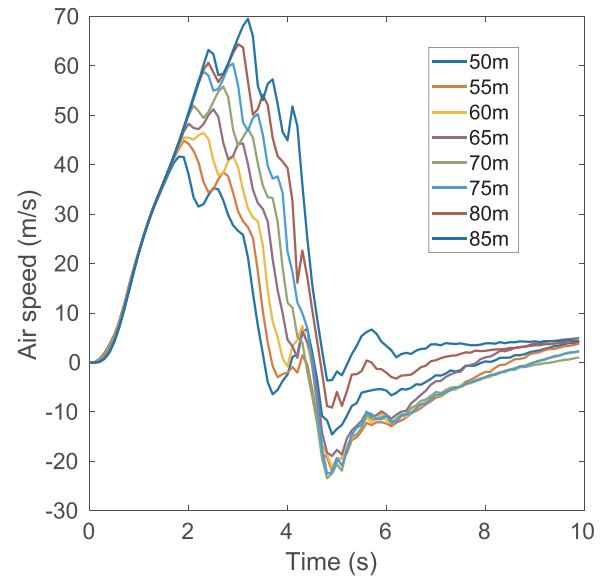


**Fig. 12.** Average airspeed in time inside the observation duct for different values of the vertical position.

similar manner.

In Fig. 13 the airspeed at the middle draw-point is observed for all the different vertical positions. It is unaffected by the vertical position and is orders of magnitude lower than the one measured at the observation duct, again due to the presence of the permeable muckpile.

In the next stage, the muckpile slope is changed and the observation duct is placed at 50 m from the domain upper end. Angles from  $10^\circ$  to  $35^\circ$  are taken. Fig. 14 shows the airspeed for the different angles, measured at the middle draw-point. As can be seen higher angles the airspeed increases. This is because the top point of the muckpile is fixed at 50 m below the falling material block. This distance is known as the air gap thickness. With this gap fixed, the angle modifies the falling distance for the rock mass and therefore for a higher angle, the falling mass gains more momentum. In all cases the speed does not surpass 10 m/s so it is still orders of magnitude less than the velocities obtained at the observation duct.

Fig. 15 shows the observation duct airspeed. For the first stage, just

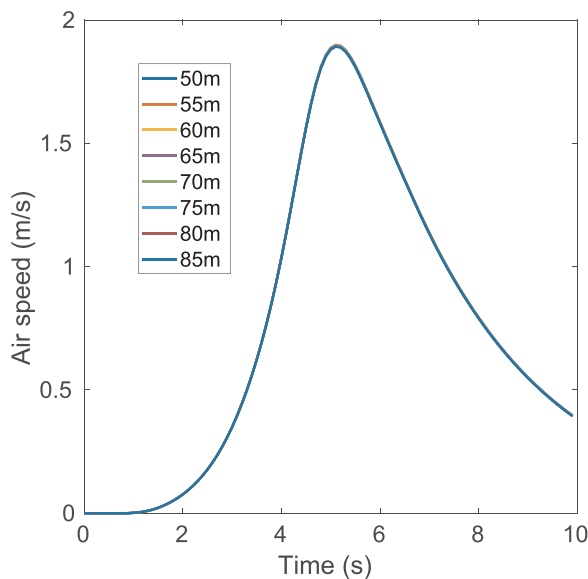


Fig. 13. Average airspeed in time inside the middle draw-point for different values of the observation duct vertical position.

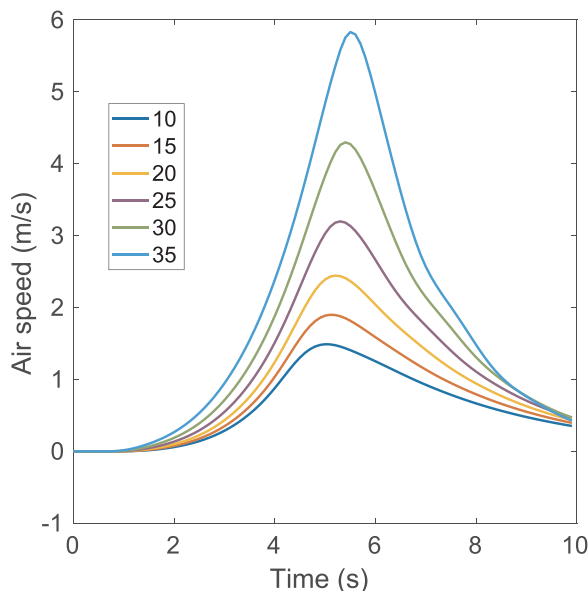


Fig. 14. Average airspeed in time inside the middle draw-point for different values of the observation duct vertical position.

after the falling mass passes the observation duct, there is no dependence on the muckpile slope. However, at higher angles, there is a second airspeed peak at around 5 s. This is a reflection from the muckpile which is aimed at the area where the observation duct is. For higher slopes, this second peak is as high as the primary one. This implies that the position of the observation duct with respect to the muckpile slope may be important in order to prevent potential hazards coming from an airblast event.

## 5. Conclusions

In this paper, a novel implementation of the coupling between DEM and LBM has been presented with a particular emphasis on the simulation of the airblast phenomena. Airblast events can occur in block caving situations where air pockets exist within the falling material. As the material falls, the air can be compressed and, if connected to any tunnel network, may be released at very high speeds.

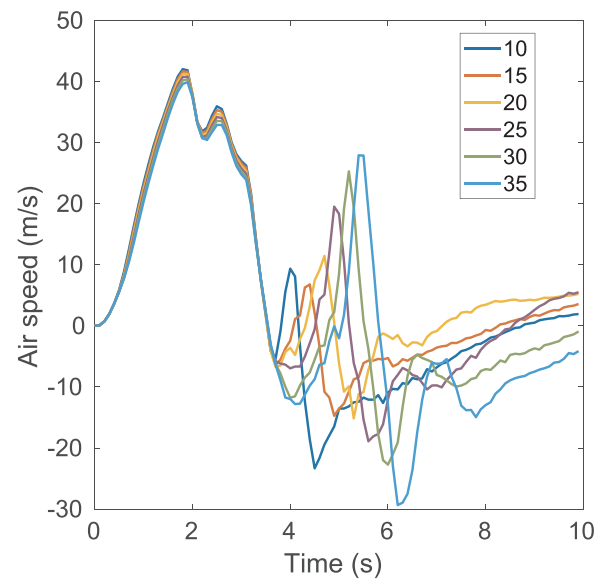


Fig. 15. Average airspeed in time inside the observation duct for different values of the muckpile slope.

Key physical phenomena associated with these events are the compression of a fluid by solid moving boundaries and the fluid-solid interaction at high velocities. It has been shown in this work how DEM-LBM is capable of dealing with these aspects with adequate accuracy. Important limits apply: In the case of the compressibility, the density cannot increase more than 10%; and in the case of the high flow velocities the Reynolds number cannot exceed  $10^5$  (measured with the drag on cylinder test) or the simulation will become inaccurate.

An experimental validation was also conducted to observe the match between the simulated airspeeds and the real ones in a scaled down lab model. The simulated airspeeds are similar, although higher, to the experimental ones. Despite the difference, they fall within an acceptable range proving the proposed simulation engine can be used to obtain realistic estimates of the airspeeds.

A simplified block caving geometry was also simulated to explore the effect of two different variables: the position of the observation duct and the muckpile slope. In both cases it was observed that the airspeed at the draw-points was considerably lower than the one measured at the observation duct. This corresponds to reports of airblast events recording high airspeeds at the observation duct and not at the draw-points. It is also shown how the position of the observation duct relative to the muck-pile is important in the mitigation of damage that the airblast event could produce.

Although further developing is needed, the results shows in this paper prove the capabilities of the DEM-LBM coupled algorithm to reproduce many of the physical phenomena involved in an airblast event at scales similar to the real block caving sites.

## Acknowledgements

The authors would like to thank Newcrest Mining Limited for the financial support on the creation and validation of this simulation tool.

## References

- Donoghue A. Occupational health hazards in mining: an overview. *Occup Med.* 2004;54(5):283–289.
- Suorineni F, Hebblewhite B, Saydam S. Geomechanics challenges of contemporary deep mining: a suggested model for increasing future mining safety and productivity. *J South Afr Inst Min Metall.* 2014;114(12):1023–1032.
- Butcher R, Stacey T, Joughin W. Mud rushes and methods of combating them. *J-South Afr Inst Min Metall.* 2005;105(11):817.
- Vejrazka C. Northparkes mines' current air blast risk assessment practices for block

- caving operations.
5. Fowler J, Hebblewhite B, Sharma P, et al., Managing the hazard of wind blast/air blast in caving operations in underground mines. In: 10th ISRM Congress, International Society for Rock Mechanics, 2003.
  6. Wu X. *Theoretical Analysis of Bump and Airblast Events Associated with Coal Mining Under Strong Roofs [Ph.D. Thesis]*. Virginia Tech; 1995.
  7. Hajihassani M, Armaghani DJ, Sohaei H, Mohamad ET, Marto A. Prediction of air-blast-overpressure induced by blasting using a hybrid artificial neural network and particle swarm optimization. *Appl Acoust.* 2014;80(Supplement C):57–67.
  8. O'Sullivan C. *Particulate Discrete Element Modelling: A Geomechanics Perspective*. Hoboken, NJ: Taylor & Francis; 2011.
  9. Oh J, Bahaaddini M, Sharifzadeh M, Chen Z. Evaluation of air blast parameters in block cave mining using particle flow code. *Int J Min Reclam Environ.* 2017;0(0):1–15.
  10. Chen Z, Yang Z, Wang M. Hydro-mechanical coupled mechanisms of hydraulic fracture propagation in rocks with cemented natural fractures. *J Pet Sci Eng.* 2018;163:421–434.
  11. Galindo-Torres S. A coupled discrete element lattice boltzmann method for the simulation of fluid-solid interaction with particles of general shapes. *Comput Methods Appl Mech Eng.* 2013;265(0):107–119.
  12. Galindo-Torres SA, Scheuermann A, Li L. Numerical study on the permeability in a tensorial form for laminar flow in anisotropic porous media. *Phys Rev E.* 2012;86:046306.
  13. Chen S, Doolen GD. Lattice boltzmann method for fluid flows. *Annu Rev Fluid Mech.* 1998;30:329–364.
  14. Feng Y, Han K, Owen D. Coupled lattice boltzmann method and discrete element modelling of particle transport in turbulent fluid flows: computational issues. *Int J Numer Methods Eng.* 2007;72(9):1111–1134.
  15. Li R, Yang YS, Pan J, et al. Lattice boltzmann modeling of permeability in porous materials with partially percolating voxels. *Phys Rev E.* 2014;90(3):033301.
  16. Korzani MG, Galindo-Torres SA, Scheuermann A, Williams DJ. Parametric study on smoothed particle hydrodynamics for accurate determination of drag coefficient for a circular cylinder. *Water Sci Eng.* 2017. <http://dx.doi.org/10.1016/j.wse.2017.06.001>.
  17. Zou Q, He X. On pressure and velocity flow boundary conditions and bounceback for the lattice boltzmann bgk model, Arxiv: <http://arXiv:9611001arXiv:9611001>.
  18. Galindo-Torres S, Pedroso D. Molecular dynamics simulations of complex-shaped particles using Voronoi-based spheropolyhedra. *Phys Rev E Stat, Nonlinear Soft Matter Phys.* 2010;81(6 Pt 1):061303.